Research Square

Preprints are preliminary reports that have not undergone peer review.
They should not be considered conclusive, used to inform clinical practice,
or referenced by the media as validated information.

A Probabilistic Agent-Based Model of Avascular Tumor Growth by Analysis of Shannon Entropy as a Phenotype Transition Index

Hamid Reza M. Zarandi

hrmz0072@gmail.com

Shahid Bahonar University

Mohammad Hassan Mollaei

Ferdowsi University of Mashhad

Farzad Sadeghi

Na. C, Islamic Azad University

Article

Keywords: Tumor Microenvironment, Cell Proliferation, Hypoxia, Biological Modeling

Posted Date: November 20th, 2026

DOI: https://doi.org/10.21203/rs.3.rs-11537827/v1

License: This work is licensed under a Creative Commons Attribution 4.0 International License.
Read Full License

Additional Declarations: No competing interests reported.

A Probabilistic Agent-Based Model of Avascular Tumor Growth by Analysis of Shannon Entropy as a Phenotype Transition Index

Hamid Reza M. Zarandi [a, 1], Mohammad Hassan Mollaei [b], Farzad Sadeghi[c]

[a] College of Physics, Shahid Bahonar University, PO Box 76175, Kerman, Iran (orcid.org/0000-0002-0037-3128)

[b] Department of Biology, Faculty of Science, Ferdowsi University of Mashhad, Mashhad, Iran

[c] Department of Physics, Na. C., Islamic Azad University, Najafabad, Iran

Abstract

A fully probabilistic, two-dimensional model has been developed to simulate avascular tumor growth. In this framework, cell proliferation, phenotype transitions, and spatial relocation of newly formed cells are governed by stochastic processes. These biological mechanisms are influenced by the local concentrations of oxygen (O_2) and carbon dioxide (CO_2) within the microenvironment, which encompasses both healthy and tumor tissues. To capture the dynamics of gas diffusion, a system of nonlinear, coupled diffusion equations for O_2 and CO_2 was numerically solved using the finite difference method on a square lattice. Based on the resulting concentration levels, cellular behavior was modeled over a 40-day period. The simulation naturally produced a multilayered avascular tumor structure, consisting of a necrotic core surrounded by concentric layers of quiescent and proliferating cells. Given the probabilistic nature of the model, Shannon entropy was employed as an index to quantify phenotype variability throughout tumor development. Findings show that quiescent and necrotic cells emerge between days 9 and 11, primarily under hypoxic conditions. By the end of simulation, the tumor reached a diameter of approximately 1–2 mm. Entropy peaked between days 11 and 13, reflecting maximal phenotypic diversity, and subsequently oscillated around an asymptotic value. This stabilization indicates a dynamic balance between cell birth and death, which may serve as an early signal of the angiogenic switch and the transition toward vascularized tumor growth.

Keywords: Tumor Microenvironment, Cell Proliferation, Hypoxia, Biological Modeling

[1] Corresponding author, Email: HRMZ0072@gmail.com

Introduction

Biological systems are complex, and many effective parameters play roles in these systems; cancer tumor is one of the most complex systems in biology because of its nature [1, 2]. Although there are some biological, chemical, and physical techniques to treat different types of cancer, but their low efficiency, high cost, invasion and the most importantly, their side effects are challenging issues in this field. Nowadays, advancements in nanotechnology have prepared new promising methods, such as targeted drug delivery, anticancer nanomaterials, and hyperthermia therapies, to encounter various cancer diseases [3-7]. Additionally, the development of computational ability has prepared this chance to model and simulate the biological complex systems such as cancer [8-11].

Some novel computational and mathematical approaches have been prepared to model the cancer tumors in different stages of growth [12-14]. Generally, a cancerous tumor has three specific stages during its growth process. The first stage is known as the avascular phase, where the initial malignant cells are proliferated and the tumor grows without any vessels. The avascular phase of the tumor is limited by its size, and as the tumor increases in size, the levels of nutrients and O_2 decrease in its center, leading to a condition called hypoxia. [9, 12, 15, 16]. The second one is the vascular phase, where the tumor starts angiogenesis owing to the hypoxia in the tumor center. In this stage, tumor cells express some genes to activate angiogenesis using endothelial cells [8, 14, 17]. In this classification, the final stage occurs when malignant cells detach from the tumor and migrate to other healthy tissues, a process known as the metastasis phase. [12, 18, 19].

The avascular phase of tumor begins with a few malignant cells, and according to the nutrient and O_2 distribution in the tissue, it typically forms a core (with necrotic cells (NCs)), an inner shell (with quiescent cells (QCs)), and an outer shell (with proliferating cells (PCs)) [14]. The NCs are a class of cell phenotype that is dead due to the deficiency of O_2 and nutrient in the center of tumor. QCs represent another cell phenotype within tumors, and although they remain alive, their activity decreases and they cannot proliferate due to the low levels of O_2 and nutrients. PCs are active cells located at the edge of tumor, and they can proliferate because sufficient nutrients and O_2 are available. Biological approach in tumor growth and phenotype change has been prepared in more detailed in section Biological background.

Simulation and modeling of the tumor were gained many considerations in the recent decades. In addition, there are some computational approaches to model tumors in various phases, for example, discrete [15, 20], continuum [21], and hybrid models [8, 10, 15]. Chaplain et. al, in 1996, prepared a mathematical framework to model a tumor in different phases [12]. Their results show that the avascular tumor radius is on the order of a few millimeters, and by using the tumor angiogenesis factor (TAF) and endothelial cells (ECs), they examined the vascular phase of solid tumors. Anderson et al studied a mathematical model for invasion and metastasis of the tumor in 1999 [18]. They reported an article with many details, and partial differential equations were used to model the tumor invasion. This study also carried out a comparison with experimental data. An

agent-based hybrid model for avascular tumor was prepared by Abajian et al in 2008 [15]. The modeling was conducted by solving numerically of diffusion equation, and the results clearly show the core/shell/shell geometry of avascular tumor. In a 3-dimensional study, in 2014, Tang et al modeled a tumor in different phases. They studied the role of drugs in the treatment as well [14]. The model is based on the diffusion equations for nutrient, waste, TAF and drug. Sadhukhan et al prepared a multi-scale and agent-based model for the growth of the avascular phase in 2021, and a cell invasion model in 2022 [10, 11]. A coupled system of some ordinary and partial differential equations has been applied in these works and they contain several biological parameters and their effects on the tumor growth.

Recent mathematical modeling efforts have addressed tumor growth dynamics from multiple complementary perspectives. A hybrid crossover model integrating integer-order, fractal-fractional, and stochastic operators was shown to capture memory effects and stochastic variability in tumor-immune interactions, reproducing clinically relevant regression patterns [22]. Meanwhile, a fractional-order cancer model revealed chaotic behaviors for both commensurate and incommensurate derivative orders, with bifurcation diagrams confirming that chaos emerges above a critical fractional order [23]. A different approach based on porous medium-type equations with uncertain parameters introduced a stochastic asymptotic-preserving scheme within a gPC-SG framework, successfully capturing finger-like projections and the evolution of proliferating, quiescent, and dead cells [24]. Finally, for a nutrient-dependent tumor model with contact inhibition, it was proven that in the absence of nutrient diffusion and cell death, the tumor patch exhibits regularizing dynamics, including contraction estimates, exponential convergence, and boundary regularity [25].

On the other hand, biological phenomena, such as phenotypic diversity, adaptive responses, neural spike trains and avascular tumor growth, are naturally stochastic and can be analyzed by entropy-based formalism [26-28]. Shannon entropy, a cornerstone of information theory, quantifies uncertainty in communication systems and has been applied to analyze complexity in biological systems, including decision theory, molecular sequence and structure analysis, cellular heterogeneity, and tumor dynamics [29-36]. Its application requires a probabilistic framework with mutually exclusive states and well-defined probabilities [37].

In this study, we introduce a completely stochastic model for avascular tumor growth. A nonlinear coupled system of diffusion equations was applied to solve the diffusion of O_2 and CO_2 in the normal and cancerous tissues. Three types of cell phenotypes were considered in this study including PCs, QCs and NCs. Then, two probabilistic viewpoints are used for determining the new location of newborn cells resulting in proliferation and phenotype changes of tumor cells. Also, the Shannon's entropy was used as index of phenotype change in tumor.

Biological background

Avascular tumors are classically regarded as the initial stage of vascular tumor development, characterized by restricted direct access of tumor cells to blood vessels [38]. This stage is

frequently observed in malignancies such as ovarian carcinoma (due to free-floating spheroid growth in ascites) and early micro-metastases (due to delayed angiogenic switching) [39]. They may develop in some locations such as cartilaginous tissues (due to inherent anti-angiogenic factors) and hypoxic niches [40]. A pivotal process in tumor progression is hypoxia, resulting from O_2 deprivation and disrupted perfusion due to the absence of the capillary network. Under these conditions, cancer cells exhibit metabolic reprogramming called the Warburg effect, secreting vascular endothelial growth factor (VEGF) to induce angiogenesis [41]. Additionally, hypoxia can change the proliferating tumor cells into quiescent cells, and these quiescent cells adopt themselves with minimal metabolic activity for survival. Consequently, O_2 depletion and waste accumulation (including CO_2) are observed in the microenvironment. O_2 deficiency exacerbates hypoxia and promotes glycolytic flux, while metabolic waste accumulation induces extracellular acidosis via biochemical activity such as carbonic anhydrase [42]. These processes inflict severe damage on cells exposed to hypoxia and waste accumulation (including CO_2). This damage drives phenotypic changes, culminating in necrosis [43].

Declining O_2 and rising CO_2 from cellular metabolism significantly increase local necrosis risk. Over time, this cascade expands the necrotic core within tumors, typically forming within 7–14 days in aggressive models [44]. Necrotic cores are documented in colorectal carcinomas and triple-negative breast tumors, reaching radii of 0.5–2.0 mm depending on metabolic rate [45]. This necrotic core is a hallmark of avascular tumors that drives tumor evolution by selecting for aggressive clones. O_2 and CO_2 gradients within the tumor microenvironment establish a chemoattractant potential. The resultant force may drive proliferating cells toward new locations, though intercellular interactions (e.g., cadherin-mediated adhesion, gap junction communication) also contribute substantially [46].

Mathematical model

In this section, we describe the stochastic model developed in this study, as a computational simulation, grounded in the inherently probabilistic nature of biological systems [1, 2]. Two fully stochastic components are incorporated: the probability of necrosis and the spatial relocation of daughter cells. These processes are modeled within a probabilistic framework that, when integrated with deterministic reaction–diffusion dynamics, allows phenotype distribution to be treated as a random variable. As a result, Shannon entropy provides a direct and natural informational index for quantifying the evolving disorder (or diversity) of the tumor cell population, thereby bridging stochastic micro-scale rules with macroscopic, measurable outcomes. Additionally, the avascular tumor structure has been divided into three distinct regions based on experimental works [47-52]. This classification is commonly adopted in the study of avascular tumor growth modeling [9, 53].

Diffusion and phenotype changes

The mathematical framework of the avascular tumor growth model has been proposed. The presented model is based on a system of two nonlinear coupled differential equations for the diffusion of O_2 and CO_2 in the tissue as follows:

$$\frac{\partial C_{O_2}}{\partial t} = D_{O_2}\nabla^2 C_{O_2} + \frac{2C_{O_2}}{C_{O_2}+C_{CO_2}}\gamma_{O_2} f(x,y)\delta(\vec{r} - \vec{r_i}) \quad (1)$$

$$\frac{\partial C_{CO_2}}{\partial t} = D_{CO_2}\nabla^2 C_{CO_2} + \frac{2C_{O_2}}{C_{O_2}+C_{CO_2}}\gamma_{CO_2} f(x,y)\delta(\vec{r} - \vec{r_i}) \quad (2)$$

where $C_{O_2}(C_{CO_2})$, $D_{O_2}(D_{CO_2})$ are the concentration, diffusion coefficient of O_2 and CO_2 and $\gamma_{O_2}(\gamma_{CO_2})$, the consumption rate of O_2 and the secretion rate of CO_2, respectively. $f(x_i, y_i) = \exp(-d_{ij}^2/2\sigma^2)$ and $d_{ij}^2 = (x_i - x_j)^2 + (y_i - y_j)^2$ is the Euclidean distance of i^{th} cell from j^{th} point in the tissue space. $\delta(\vec{r} - \vec{r_i})$ is Dirac delta function, it is one if $\vec{r}$ be the i^{th} cell place and it is 0 otherwise. The Gaussian function appearing in the source terms, serves both a biological and a mathematical purpose. Biologically, a living cell is not a point source; its consumption of oxygen and secretion of carbon dioxide occur across its entire volume and extend into the surrounding extracellular matrix due to diffusion across the cell membrane. The Gaussian kernel therefore represents the spatial footprint of a single cell's metabolic activity, with the characteristic width σ chosen to be on the order of a typical cell diameter (here $\sigma = \Delta x$, the grid spacing). Mathematically, the convolution of a Dirac delta with a Gaussian yields a smooth approximation of a point source – a standard technique in cell-based and agent-based models to avoid singularities and ensure numerical stability [54]. As σ→0, the Gaussian tends to the delta function, recovering the original point-source formulation. The negative sign in the exponent ensures that the influence decays with distance from the cell, which is physically realistic. The term $2C_{O_2}/(C_{O_2} + C_{CO_2})$, follows a Michaelis-Menten-type competition kinetics, reflecting that oxygen consumption and carbon dioxide production are coupled by metabolic stoichiometry [55]. These equations were solved by finite difference method (FDM) with Dirichlet boundary conditions on a square with length $L = 5$ mm. The initial conditions are the standard levels of O_2 and CO_2 in the tissue obtained from [14]. There are only three cell phenotypes, including NCs, QCs, and PCs. It was assumed that the NCs are fixed at their places, so they are not allowed to move in the microenvironment and the cell movement has been only considered for the PCs and QCs. The variations between phenotypes are Q → P, P → Q and Q → N for quiescent into proliferating, proliferating into quiescent, and quiescent into necrotic, respectively. Also, there is no possibility for NCs to change into other phenotypes. The variations in phenotype were done according to the changes in O_2 and CO_2 concentrations using these mathematical rules inspired form biological concepts.

The doubling time of each cell was set for 24 h, and the cell phenotype is updated at the end of each day. The phenotype change, as mentioned above, is carried out using a stochastic and probabilistic mechanism. Based on this model, the concentration of O_2 was calculated for all cells, and its average is obtained at the end of every day. When the average of O_2 level in the tumor area

decreases under 30%-50% of the initial level, the initial condition for phenotype change from PCs to QCs is satisfied. Now, there are two conditional statements that reflect a dynamic mechanism to change these phenotypes to each other, as follows:

As first condition, $m = 2C_{O_2}/(C_{O_2} + C_{CO_2})$ is defined as a criterion of cell metabolism. Also, $R_{eff}^{P\leftrightarrow Q}$, effective metabolic radius (EMR), is obtained using the following equation:

$$R_{eff}^{P\leftrightarrow Q} = \frac{\sum_{i=1}^{N_P} r_i^P \alpha^P m_i^P + \sum_{j=1}^{N_Q} r_j^Q \alpha^Q m_j^Q}{\sum_{i=1}^{N_P} \alpha^P m_i^P + \sum_{j=1}^{N_Q} \alpha^Q m_j^Q} \quad (3)$$

where $r_{i(j)}^{P(Q)}$, $m_{i(j)}^{P(Q)}$, $\alpha^{P(Q)}$ and $N_{P(Q)}$, are the radius of $i^{th}(j^{th})$ cell from origin, the metabolism of $i^{th}(j^{th})$ cell, cell activity, and the number of proliferating and quiescent cells, respectively. In this stage, the radius of each cell (r_i) is compared to $R_{eff}^{P\leftrightarrow Q}$and,

$$\begin{cases} \text{if} \quad r_i \le R_{eff}^{P\leftrightarrow Q} \quad \Rightarrow \quad P \to Q \\ \text{if} \quad r_i > R_{eff}^{P\leftrightarrow Q} \quad \Rightarrow \quad Q \to P \end{cases}. \quad (4)$$

For the second one, we pursue the probabilistic approach by defining the $\Delta_i^{P\leftrightarrow Q}$ as

$$\Delta_i^{P\leftrightarrow Q} = \frac{\beta_{O_2} C_{O_2} - \beta_{CO_2} C_{CO_2}}{\beta_{O_2} C_{O_2} + \beta_{CO_2} C_{CO_2}} \quad , \quad C_{O_2} > C_{CO_2} \quad (5)$$

where $\beta_{O_2(CO_2)}$ are estimated by the obtained results in the modeling process. Then, we choose a random number, $\xi_i^{P\leftrightarrow Q} \in [0, 1]$, based on the normal distribution function, $N(p_i, \sigma_\Delta)$, where $p_i = \Delta_i^{P\leftrightarrow Q}/\Delta_{max}^{P\leftrightarrow Q}$, and σ_Δ stands for the standard deviation of $\Delta_i^{P\leftrightarrow Q}$. The threshold of $P \leftrightarrow Q$ phenotype change is $\delta_{th}^{P\leftrightarrow Q}$. Now,

$$\begin{cases} \text{if} \quad \xi_i^{P\leftrightarrow Q} \le \delta_{th}^{P\leftrightarrow Q} \quad \Rightarrow \quad P \to Q \\ \text{if} \quad \xi_i^{P\leftrightarrow Q} > \delta_{th}^{P\leftrightarrow Q} \quad \Rightarrow \quad Q \to P \end{cases}. \quad (6)$$

The phenotype changes between PC and QC is done if both conditions are true. The same approach is applied for $Q \to N$ phenotype change with substituting P and Q with Q and N, respectively, and considering $\Delta_i^{Q\to N} = -\Delta_i^{P\leftrightarrow Q}$ when $C_{O_2} < C_{CO_2}$.

The phenotype transition rules defined in Eqs.(3-6), are derived from two complementary biophysical principles: a deterministic mechanical-metabolic criterion based on an effective metabolic radius $R_{eff}^{P\leftrightarrow Q}$, and a probabilistic chemical-gradient criterion based on local oxygen-to-carbon dioxide ratios. The deterministic component (Eqs(3-4)) captures the observation that cells farther from the tumor center (larger radius r_i) experience different mechanical and nutrient microenvironments, which influences their proliferative state [56]. The weighting by cell activity $\alpha^{P(Q)}$ and metabolism $m_i^{P(Q)}$ accounts for the fact that more metabolically active cells

contribute more to the effective radius. The probabilistic component (Eqs.(5-6)) introduces stochasticity inherent in cellular decision-making, where $\Delta_i^{P\leftrightarrow Q}$ represents a normalized difference between oxygen and carbon dioxide concentrations, reflecting the idea that a high oxygen-to-waste ratio favors proliferation, while a low ratio favors quiescence [57]. The use of a normally distributed random variable $\xi_i^{P\leftrightarrow Q}$ with mean p_i (scaled local gradient) and standard deviation σ_Δ (derived from the population variance) mimics the biological variability observed in clonal cell populations under identical external conditions [58]. Whereas we set $\delta_{\text{th}}^{P\leftrightarrow Q} = \delta_{\text{th}}^{Q\to N} = 0.5$ as a baseline binary decision logic (i.e., equal probability of switching when the normalized gradient is at the population mean), we recognize that this choice could appear arbitrary. To address this, in Sec.(4) (or as summarized in Tabs(2-3)) we systematically varied both thresholds over a range of values (e.g., $\delta_{\text{th}}^{P\leftrightarrow Q} = 0.7$, $\delta_{\text{th}}^{Q\to N} = 0.3$) and examined the resulting tumor dynamics. The outcomes demonstrate a clear tolerance to these variations: final tumor diameter, cell type percentages, and total cell numbers changed only marginally (less than 10 percent across cases). Thus, while the binary threshold of 0.5 serves as a convenient and interpretable baseline, the model's predictions are robust to moderate deviations, confirming that the thresholds are not critical free parameters but rather reflect a universal insensitivity of tumor progression to small changes in phenotype switching rules. The same rationale applies to the Q→N transition, with the sign reversal of Δ_i reflecting the fact that waste dominance drives necrosis. Finally, requiring both conditions to be true for a phenotype change ensures that a cell must experience both a mechanical-metabolic imbalance (via R_{eff}) and a chemical-gradient bias (via ξ_i) before switching.

Cell movement

Based on the chemotactic mechanism mentioned above, the cell movement and tumor growth were modeled by defining two forces for O_2 and CO_2 resulting from their diffusions, as the following equations:

$$\mathbf{F_{O_2}} = -\mathrm{k}_{\mathrm{O}_2}\boldsymbol{\nabla}\mathrm{C}_{\mathrm{O}_2} \tag{7}$$

$$\mathbf{F_{CO_2}} = \mathrm{k}_{\mathrm{CO}_2}\boldsymbol{\nabla}\mathrm{C}_{\mathrm{CO}_2} \tag{8}$$

where $\mathrm{k}_{\mathrm{O}_2}$ and $\mathrm{k}_{\mathrm{CO}_2}$, are two constants. Also, based on the normal distribution function, $\mathrm{N}(\theta, \sigma_\theta)$, in which $\theta = \tan^{-1}\left(\left(\mathrm{F}_{\mathrm{O}_2}^{\mathrm{y}} + \mathrm{F}_{\mathrm{CO}_2}^{\mathrm{y}}\right)/\left(\mathrm{F}_{\mathrm{O}_2}^{\mathrm{x}} + \mathrm{F}_{\mathrm{CO}_2}^{\mathrm{x}}\right)\right)$, $\sigma_\theta \in \left(\frac{\pi}{6}, \frac{5\pi}{6}\right)$ and the new location is obtained from these equations

$$\mathrm{x}_{\mathrm{new}} = \mathrm{x}_{\mathrm{old}} + 2\mathrm{r}_{\mathrm{cell}}\cos\phi \tag{9}$$

$$\mathrm{y}_{\mathrm{new}} = \mathrm{y}_{\mathrm{old}} + 2\mathrm{r}_{\mathrm{cell}}\sin\phi \tag{10}$$

where $\phi \in [0, 2\pi]$ is a random angle from N, and (x_{old}, y_{old}) is the coordinate of the mother cell, and the two daughter cells are located at (x_{old}, y_{old}) and (x_{new}, y_{new}). All parameters used in the modeling and their values were summarized in Table 1. Also, Figure 1 shows the algorithm flowchart of the model.

The cell movement model defined by Eqs(7-10) captures the essential chemotactic responses to oxygen and carbon dioxide gradients while deliberately keeping the description at a minimal, computationally efficient level. Forces are taken proportional to the gradients of the two chemical species, with opposite signs to reflect that cells move toward higher oxygen (chemoattraction) and away from higher carbon dioxide (chemorepulsion) [59]. Although a more detailed description could include cell-cell adhesion, haptotaxis, or mechanosensing, the present formulation has been successfully used in some multiscale tumor models to reproduce experimentally observed migration patterns [60, 61]. The inclusion of a normally distributed random angle ϕ with mean direction θ (computed from the resultant chemotactic force) and standard deviation σ_θ accounts for the inherent randomness in cell locomotion due to membrane fluctuations, receptor noise, and local microenvironmental heterogeneities [62]. The selection of the angular standard deviation σ_θ is grounded in the experimental data reported in [63], who observed that MOS-11 cells migrating in a three-dimensional collagen lattice exhibit a bimodal distribution of inter-step turning angles, with pronounced peaks at approximately 30° and 150° on either side of the previous direction. This pattern arises from the alternating ruffling activity of the bipolar cell membrane and indicates that the cells are capable of both small, persistent turns as well as large, nearly reversing turns. The value σ_θ = π/4 (45°) corresponds to a moderate angular spread that encompasses the 30° peak while still allowing occasional larger deviations. Similarly, σ_θ = π/2 (90°) provides a broader spread that covers the range between the two experimental peaks, thereby capturing the full spectrum of observed turning behavior without restricting the cells to either extreme. Both σ_θ = π/4 and σ_θ = π/2 consistently yield rounded tumor boundaries (cases D and B in Tab.(3)), demonstrating that the preservation of a smooth, spherical morphology does not require an excessively large angular spread. In contrast, reducing σ_θ to near zero forces the cells to move in an almost ballistic manner (unrealistic for the experimental system), whereas further increasing σ_θ to 3π/4 (135°) does not substantially improve the morphological outcome. Therefore, the choices σ_θ = π/4 and π/2 are directly justified by the empirical turning-angle distribution of [63] and by their ability to faithfully reproduce the rounded tumor shape observed in the experimental and simulation results.

Table 1. Numerical values of parameters applied in modelling

Symbol	Value	Unit	Description	Reference
$\mathbf{D_{O_2}}$	5.0×10^{-9}	m^2/s	O_2 diffusion constant	[64]
$\mathbf{D_{CO_2}}$	5.0×10^{-9}	m^2/s	CO_2 diffusion constant	[65, 66]
$\boldsymbol{\gamma_{O_2}}$	1.0×10^{-3}	$\mathrm{mol}/(\mathrm{m}^3.\mathrm{s})$	O_2 consumption rate	[67]
$\boldsymbol{\gamma_{CO_2}}$	1.0×10^{-4}	$\mathrm{mol}/(\mathrm{m}^3.\mathrm{s})$	CO_2 production rate	[68]
$\bar{\mathbf{C}}_{\mathbf{O_2}}$	8.4	$\mathrm{mol}/\mathrm{m}^3$	Standard nutrient concentration	[14]
$\bar{\mathbf{C}}_{\mathbf{CO_2}}$	10.5	$\mathrm{mol}/\mathrm{m}^3$	Standard waste concentration	[14]
$\boldsymbol{\alpha^P}$	1.0	–	Proliferative cell activity	Estimated
$\boldsymbol{\alpha^Q}$	0.3	–	Quiescent cell activity	Estimated
$\boldsymbol{\alpha^N}$	0.0	–	Necrosis cell activity	Estimated
$\boldsymbol{\beta_{O_2}}$	1.0	–	O_2 probabilistic constant	Estimated
$\boldsymbol{\beta_{CO_2}}$	1.0	–	CO_2 probabilistic constant	Estimated
$\boldsymbol{\delta_{th}^{P\leftrightarrow Q}}$	0.5	–	The threshold of transition between P and Q	Estimated
$\boldsymbol{\delta_{th}^{Q\rightarrow N}}$	0.5	–	The threshold of transition of Q to N	Estimated
$\mathbf{k_{O_2}}$	0.11	$(\mathrm{kg}.\mathrm{m}^5)/(\mathrm{mol}.\mathrm{s}^2)$	Chemotaxis-like constant of O_2	Estimated
$\mathbf{k_{CO_2}}$	0.09	$(\mathrm{kg}.\mathrm{m}^5)/(\mathrm{mol}.\mathrm{s}^2)$	Chemotaxis-like constant of CO_2	Estimated
$\boldsymbol{\sigma_\theta}$	$3\pi/4$	radian	Uncertainty in movement angle	Estimated
$\mathbf{r_{cell}}$	20.0	μm	Tumor cell radius	Estimated

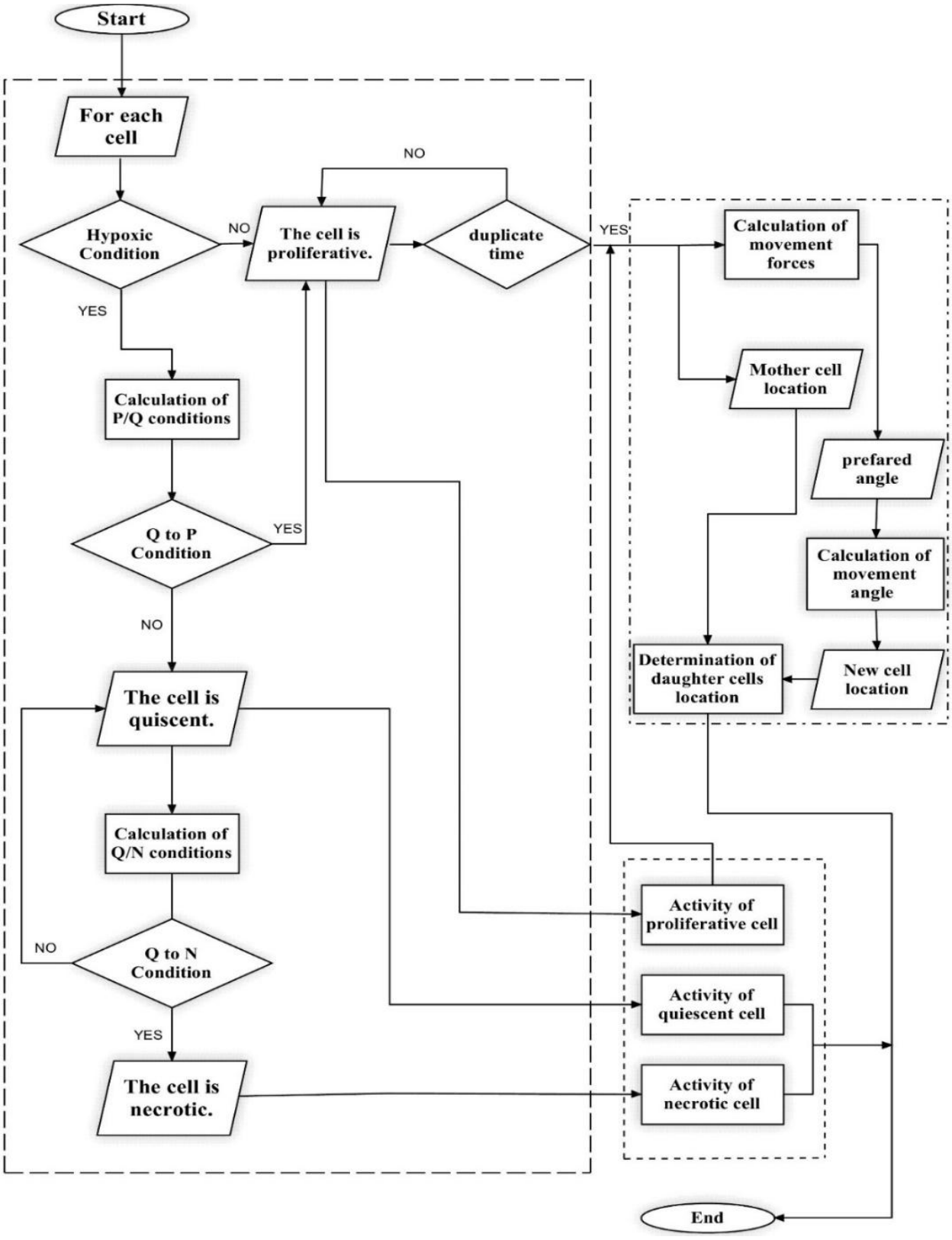


Fig. 1. Flowchart of our presented model in this study

Phenotype change index

Phenotypic entropy is defined using Shannon's formalism. At 24-hour intervals, the cell population $\hat{S}_C$ is partitioned into three separated subsets: proliferating ($\hat{S}_{PC}$), quiescent ($\hat{S}_{QC}$), and necrotic subset ($\hat{S}_{NC}$), ensuring each cell occupies a single phenotype at the coordinate (x_i, y_i). Phenotype probabilities are computed as $P_k(t) = n(\hat{S}_k)/n(\hat{S}_C)$. The Shannon's entropy for phenotypic heterogeneity is:

$$H_{Ph}(t) = -\sum_{j=PC,QC,NC} P_j(t) \log_2 \left(P_j(t)\right). \quad (11)$$

Minimum and maximum values are zero in the initial conditions when all cells are proliferating and 1.58 bits under uniform cell populations, respectively. In addition, $H_{Ph} \to 0$ if one phenotype dominates. The maximum entropy shows the maximal uncertainty, as derived via constrained optimization [69].

Results and Disscusion

In this section the obtained results have been discussed. The modeling of avascular tumor growth was carried out for 50 days. The initial number of cancerous cells was 5 at $t = 0$. Also, the doubling time, time duration of cell division, was set for one day (24 h). These initial cells are proliferating and were located on a circle at the center of the modeling region. Biologically viewpoint, the phenotype of the cells after division will vary, by using the concentration of O_2 and CO_2 in the microenvironment. Thus, tumor growth morphology and number of cells affect the O_2 and CO_2 concentration during growth.

To deeply understand this growth model, Figure 2 illustrates the spatial evolution of the metabolic function, $m = 2C_{O_2}/(C_{O_2} + C_{CO_2})$, for six days. The results reveal a dynamic governing phenotypic transition in avascular tumors. Initial homogeneity, at day 5, shows uniformly high values ($m \approx 2.0$) owing to low contribution of CO_2 in the tissue. Also, the contribution of CO_2 is one-tenth of O_2 in this model. So, the dominant contribution of this function is related to its numerator. When the CO_2 enhances in the tumor tissue, the value of m initiates to decrease and it approaches to one in the tumor center on 9th day. This trend will be kept with tumor growth. With increase in the necrotic region, the accumulation of CO_2 happens in the outer shells, where there is the maximum of O_2 consumption and the minimum CO_2 secretion in the tumor, while the value of m gradually approaches to the constant value (a little more than one) in the necrotic core (Figure 2d, e, and f). The darker regions in Figure 2 can be also explained by non-uniform distribution of proliferating and quiescent cells in the tumor tissue.

Figure 3 shows the results of tumor growth at six different days (5, 9, 15, 20, 30, 40). In Figure 3, the proliferating, quiescent, and necrotic cells are colored red, yellow, and blue, respectively. The number of cells increases using the proliferating cells in the enough presence of O_2 in the tissue. Figure 3a shows the 5th day of the modeling, when the cell number increases by 80 and all cell are

proliferating. This way is kept till 8th day due to enough O_2 in the tissue. The 9th day is when some cells experience the low level of O_2 and the hypoxia happens for some cells at the center of tumor and some ones change to the quiescent cells (yellow part of Figure 3b).

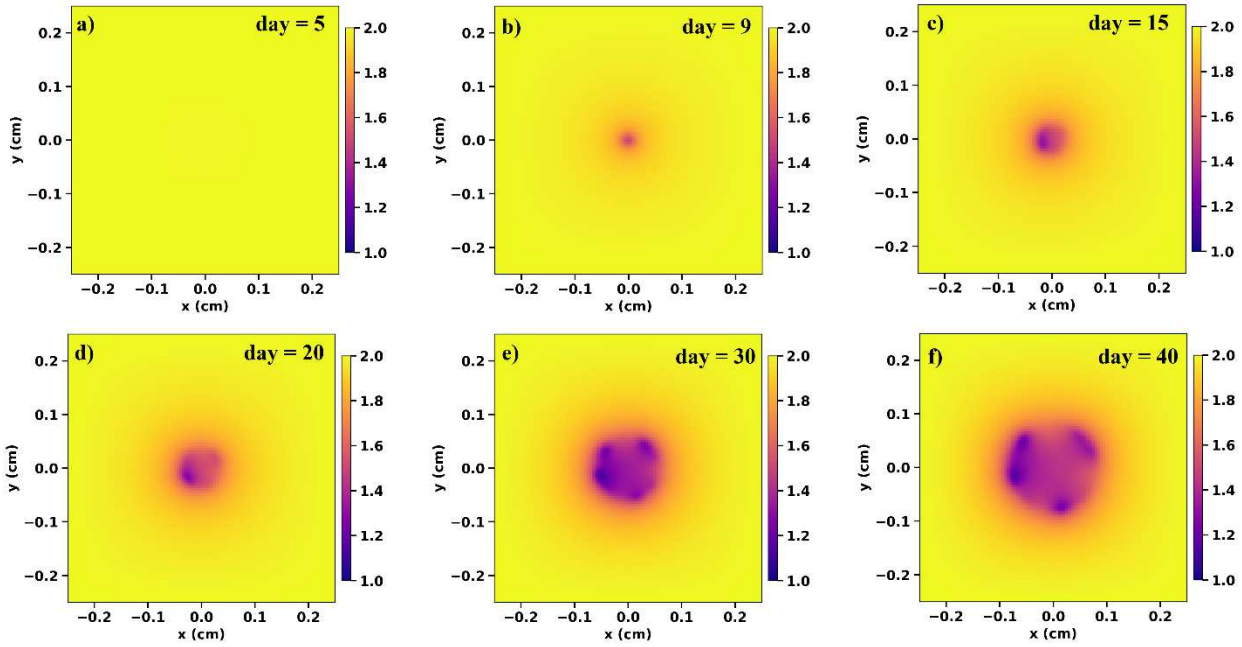


Fig. 2. Diffusion of metabolism function after a) 5, b) 9, c) 15, d) 20, e) 30, and f) 40 days.

This hypoxia preserves and enhances with increase in cell number and when the O_2 concentration decreases under a threshold level ($\delta_{th}^{Q\rightarrow N} = 0.5$), some cells are necrosed (bule area in Figure 3c). The necrotic cells are observable at 15th day in this model. Based on literature, this morphology of avascular tumor can be kept for several weeks (about 4 to 8 weeks), and the size of the tumor diameter maximally increases by 1-2 mm [9, 70-72]. Thus, this trend of growth can continue for days. The contribution of necrotic cells will strongly enhance due to the expansion of tumor size, where the O_2 level decreases and the CO_2 level increases in the tumor microenvironment.

Figure 3d-f illustrates the development of the tumor. According to the presented model, the tumor radius approaches to 1 mm at the 40th day, can be verified by experimental and modeling data prepared in previous works [73]. The location of cells at each stage will be updated based on the off-lattice pattern presented above. Taking the probabilistic and stochastic framework of the prepared model into account, the tumor shape in the initial days is approximately asymmetric, and gradually it obtains a circular core/shell/shell morphology. This result, additionally, is in agreement with the results in literature [17, 72].

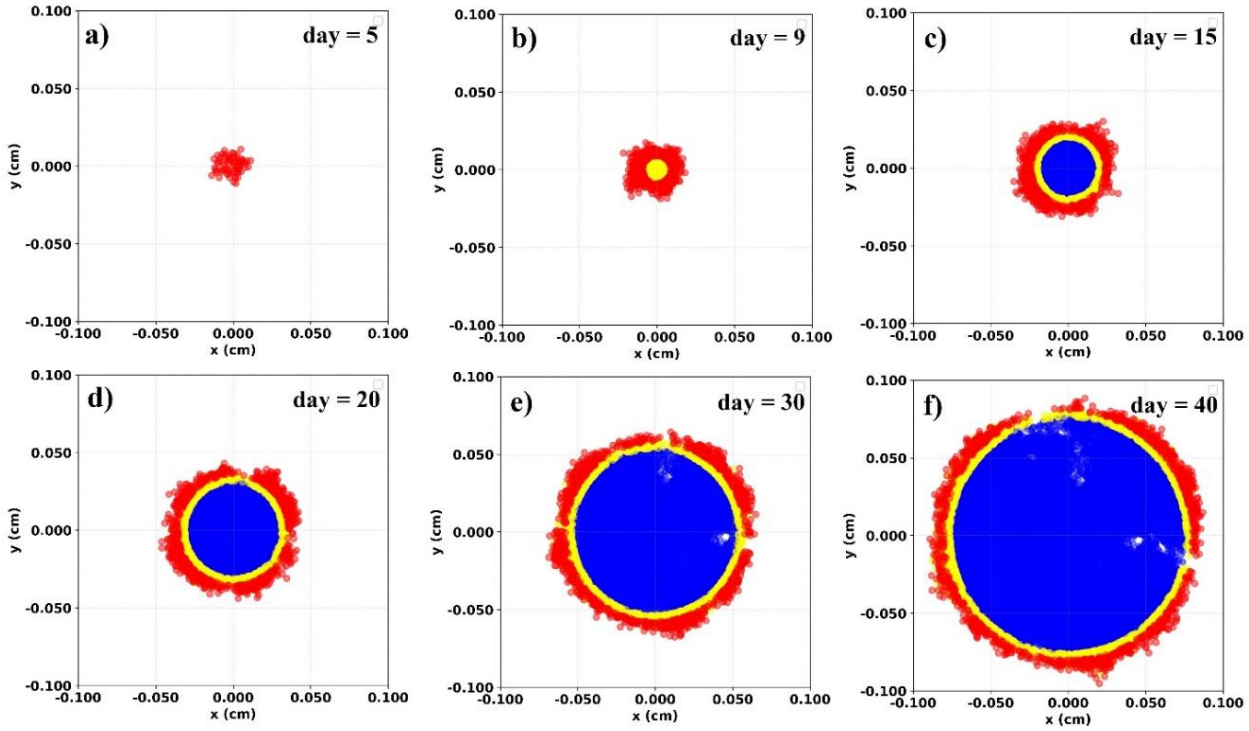


Fig. 3. Spatial tumor growth and cell distribution with different phenotypes after a) 5, b) 9, c) 15, d) 20, e) 30, and f) 40 days. The blue, yellow, and red regions, respectively, show the NCs, QCs, and PCs.

Figure 4 shows the diffusion of O_2 in the microenvironment after 10, 20, 30, and 40 days. Since the source of O_2 is located on the boundaries of the square and O_2 is consumed at the center, the low concentration area increases in the center, confirming the growth tumor process. Dark blue color in the center of these graphs (Figure 4) illustrates the high density of proliferating and quiescent cells in the initial days (hypoxic area). When the tumor starts the necrosing process and the core/shell/shell configuration of the tumor forms, the O_2 level decreases in the central area owing to O_2 consumption by proliferating and quiescent cells in the shells.

Additionally, because of the stochastic nature of the model, the tumor growth is not uniform, and the density of proliferating cells varies in different directions. Thus, the dark blue points in the density plots are completely non-uniform (Figure 4). Also, the O_2 concentration vanishes, and the asymmetric shape of this region can be explained by the non-uniform distribution of tumor growth. Since the supplementary of O_2 is effectively carried out in the close of the boundaries, the diffusion will get a spherical symmetric shape when the tumor size increases. The area with the high concentration of O_2 (blue color) has approximately the same size as the tumor size reported in Figure 3.

The proliferating and quiescent cells, owing to metabolism, consume O_2 and produce CO_2. Figure 5 shows the diffusion of CO_2 generated by cells. According to the results, the CO_2 accumulates in the center of region. Also, the boundaries of square have been considered as the sink of CO_2. Prepared Figure 5 shows the accumulation of CO_2 during the tumor growth process. Figure 5a

shows the CO_2 diffusion on the 10th day, and the maximum concentration is about 0.06, regarding proliferating and quiescent cells. Increasing in tumor radius, in the next days, shows the higher accumulation of CO_2 in the center region (red color areas). This result can be described by the boundary condition of CO_2 diffusion equation since the CO_2 produced in the metabolism of quiescent and proliferating cells in the shells of the tumor can diffuse in all directions. The asymmetric shape of diffusion has the same reason, explained earlier for O_2. Here, and in a similar way with O_2, the radius of the tumor is almost the same as the high concentration region of CO_2.

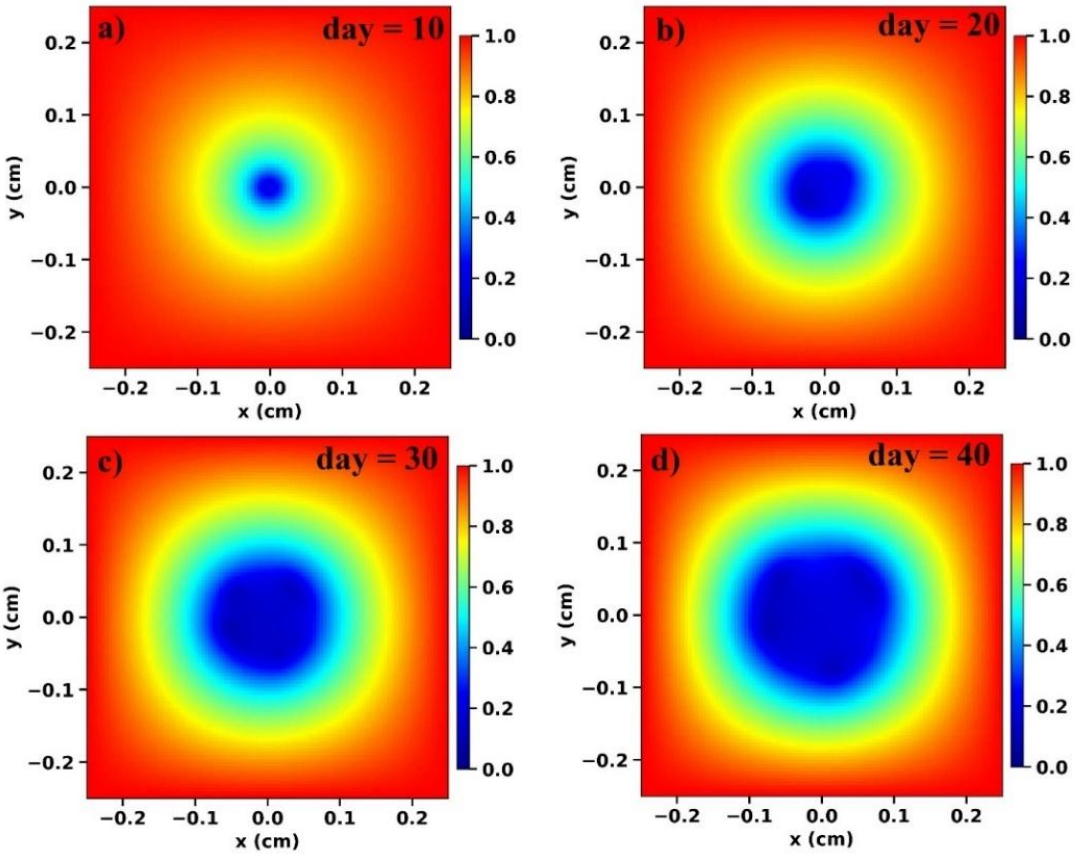


Fig. 4. Diffusion of O_2 concentration after: a) 10, b) 20, c) 30 and d) 40 days.

Figure6 shows the average of O_2 and CO_2 levels in the tumor tissue (in the other word, the average of O_2 and CO_2 concentration at each cell) on each day. The concentration of O_2 strongly decreases by the 8th day, and its value drops below 0.3, where the quiescent condition, on the 9th day, is satisfied. Then, the average of O_2 level in tumor tissue is approximately constant and lower than 0.2 (Figure 6a). In contrast, the average of CO_2 shows a sharp increase by 9th day and after that it fluctuates between 0.06 and 0.07 (Figure 6b). It can be described using the same rate of proliferating and necrosis which can be observed below in Figure 8 related to Shannon's entropy too. The stability of O_2 and CO_2 are clearly in agreement with the tumor growth shapes in Figure 3. These constant values confirm conditions determined for cell movement and phenotype change

in the model. In addition, this stability of O_2 and CO_2 is the reason for keeping of the core/shell/shell structure of the tumor during the growth.

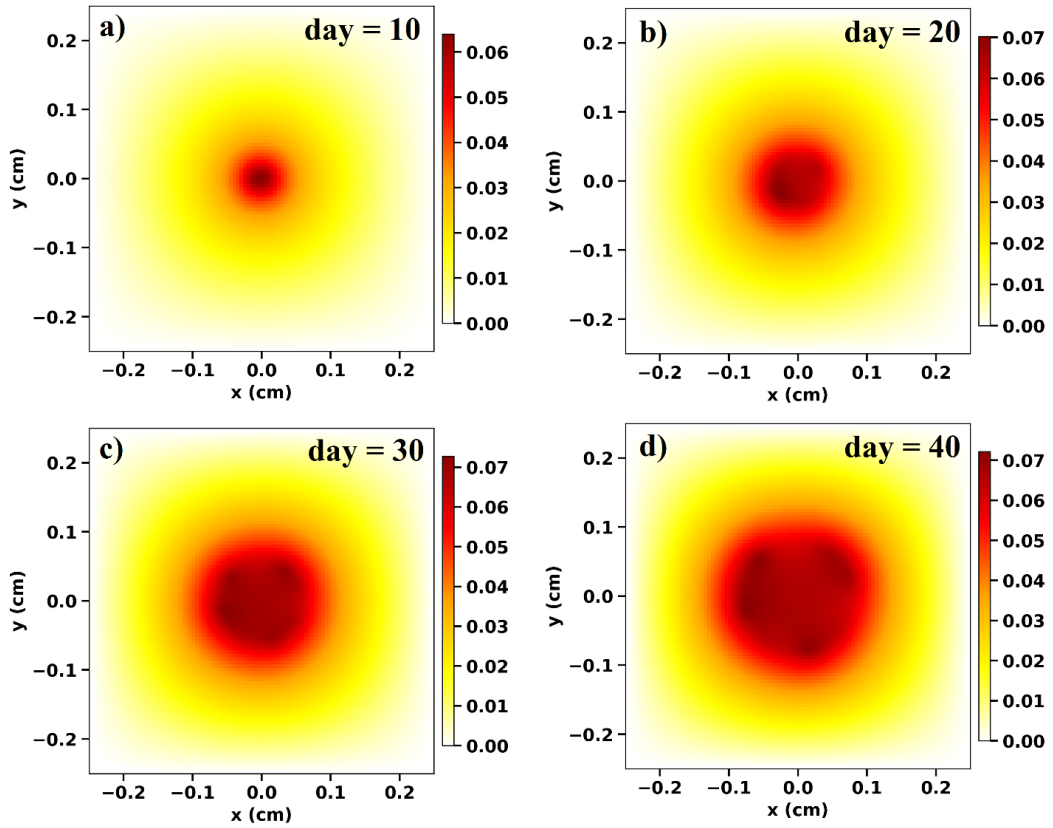


Fig. 5. Diffusion of CO_2 concentration after: a) 10, b) 20, c) 30, and d) 40 days.

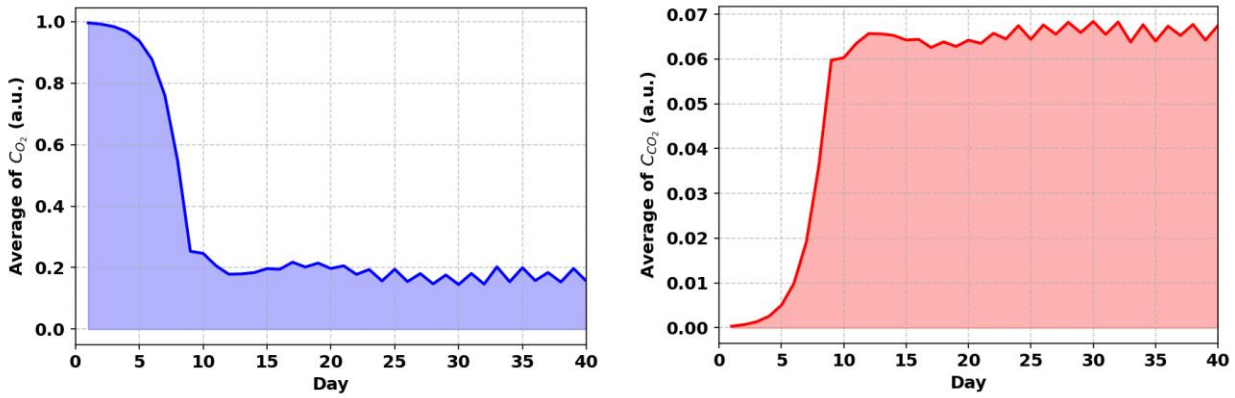


Fig. 6. The variation of the average of a) O_2 and b) CO_2 concentrations in the tumor tissue with tumor growth (at each day).

The variation of cell numbers and the change in defined phenotype entropy have been exhibited in Figure 7. As mentioned above, the necrotic cells form the largest area of the tumor after a sharp

decline in O_2 level throughout the tumor. Figure 7 shows that the number of quiescent and necrotic cells is zero, and only the number of proliferating cells increases using cell division. When the hypoxic condition occurs in the tumor, the number of quiescent and proliferating cells becomes approximately constant and the same, while the number of cells in the necrotic core strongly increases. The total cell number at the latest days of growth is around 4×10^4. The observed results can be verified by different works in the literature [14, 16, 53].

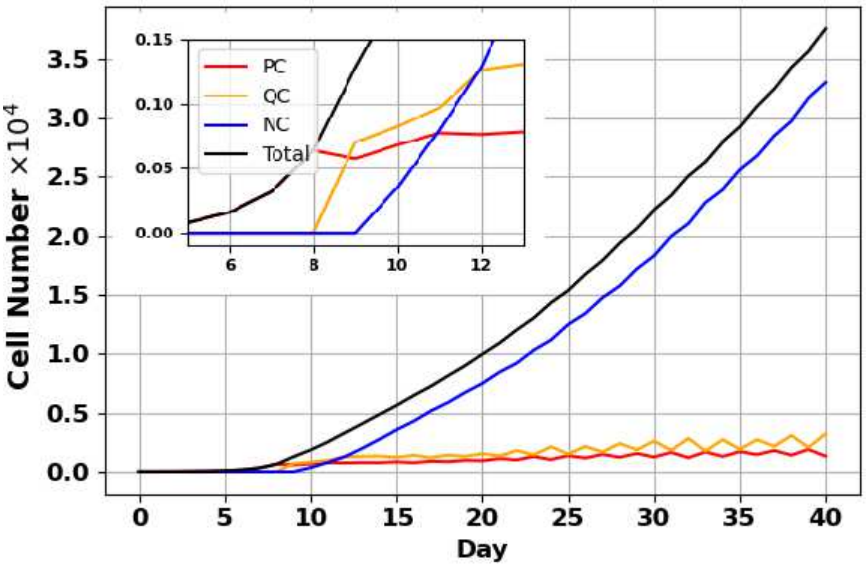


Fig. 7. Evolution of cell number by phenotype

Table 2. introducing the different conditions in modeling

Case	σ_θ	$\delta_{th}^{P\leftrightarrow Q}$	$\delta_{th}^{Q\rightarrow N}$
A	$3\pi/4$	0.5	0.5
B	$\pi/2$	0.5	0.5
C	$\pi/2$	0.7	0.3
D	$\pi/4$	0.5	0.5
E	$\pi/4$	0.7	0.3

Table 3. comparison of the obtained results for different conditions in the modeling

Case	Day	D (mm)	Proliferating cells (%)	Necrotic cells (%)	Total cell numbers
A	5	0.2696	100	0	8.0×10^1
	20	0.8368	9	75	1.0×10^4
	40	1.5772	3	88	3.7×10^4
B	5	0.2772	100	0	8.0×10^1
	20	0.9244	10	73	1.1×10^4
	40	1.9320	4	88	3.8×10^4
C	5	0.2772	100	0	8.0×10^1
	20	0.9072	8	72	1.1×10^4
	40	1.8594	4	86	4.0×10^4
D	5	0.3664	100	0	8.0×10^1
	20	1.1344	8	70	1.5×10^4
	40	2.2800	4	85	5.6×10^4
E	5	0.3664	100	0	8.0×10^1
	20	1.1330	9	70	1.6×10^4
	40	2.2746	4	85	6.0×10^4

The evolution of $H_{Ph}(t)$ (or PCI) delineates three tumor growth phases (Figure 8a). From days 0–8, entropy remains zero because there are only PCs in the tumor (Figure 7). Days 8–12 exhibit a sharp increase in entropy, peaking near 1.58 bits, driven by hypoxia-induced transitions from proliferation to quiescence and necrosis due to O_2 deprivation and CO_2 accumulation [19, 74]. This peak signifies maximal phenotypic heterogeneity [20, 75, 76]. Beyond day 12, entropy declines smoothly as necrosis predominates, culminating in a dynamic equilibrium in the balance of proliferating and necrosing rates [76]. It seems that $H_{Ph}(t)$ shows the asymptotic behavior and $dH_{Ph}/dt \rightarrow$ constant. This result correlates with the phenotypic transition rate, modulated by hypoxia gradients and metabolite trend [77, 78]. To assess the stability and reproducibility of the model, we considered five cases (involving different values for the model parameters) in Table 2 and presented their results in Table 3. We will further examine these results in the next section (Discussion).

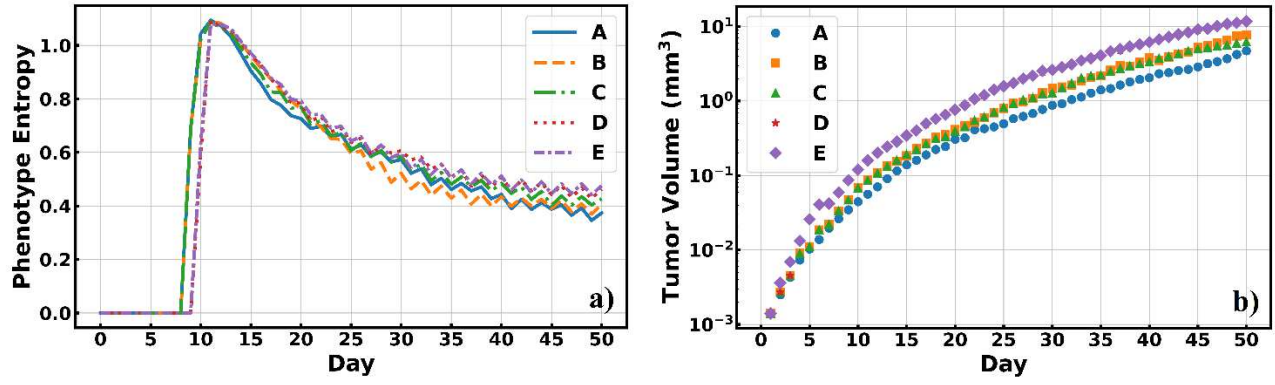


Fig. 8. Evolution of a) cell number by phenotype, b) PEI, during the tumor growth.

Notes on Computational Setup

This entropy framework distills complex tumor evolution into a succinct metric, applicable for monitoring tumor growth trends by estimating the relative frequency of phenotypes. Under the parameter ranges explored in this study, the entropy trend exhibits a qualitatively consistent pattern, as shown in Figure 8a. However, the exact values and the rate of approach to the plateau can vary with model parameters; thus, the trend is not strictly universal but rather robust within the tested conditions. The entropy peak can be considered as a criterion of phase transition from avascular to vascular phase for tumor growth. Then, it falls down and moves toward an oscillating behavior around an asymptotic value that is the subsequent of equilibrium of death and birth in the tumor cell [52]. It can be considered as the end of avascular phase of tumor growth and a sign angiogenesis emergence.

The computational implementation couples the continuous reaction-diffusion equations on a fixed Cartesian grid (101×101 points, $\Delta x \approx 0.005$ mm) with off-lattice agent-based cell dynamics. The diffusion terms are discretized using a five-point stencil and integrated explicitly with a fixed time step $\Delta t = 0.2$ s, which satisfies the Courant stability condition. The key on-lattice / off-lattice coupling is resolved in two ways: (i) to map the discrete cell positions onto the grid, each non-necrotic cell contributes to the cell mask via a Gaussian kernel of width $\varepsilon = \Delta x$ (weighted by 1 for proliferative, 0.3 for quiescent), which smoothly spreads the metabolic activity over several grid points and avoids point-source singularities; (ii) conversely, whenever a cell requires the local concentration of oxygen or waste (for phenotype classification, chemotactic force calculation, or birth events), the value is obtained by bilinear interpolation from the four nearest grid points using the function *interp*. This two-way coupling ensures that cells moving continuously in space correctly sample the diffusive fields without being restricted to grid nodes. Cell division occurs once per day for all proliferative cells: a daughter cell is placed at a distance $2r_{\text{cell}}$ ($r_{\text{cell}} = 0.002$ mm) from the mother in a direction determined by the local chemotactic force (computed from interpolated O_2 and CO_2 gradients) plus a normally distributed angular noise with standard deviation $\sigma_\theta = 3\pi/4$. No explicit collision detection is implemented; the small division distance combined with the random angular spread naturally prevents systematic cell overlap, and the Gaussian smoothing of the mask makes the source terms robust even if two cell centres come very close. The explicit time stepping is stable ($\Delta t \leq \Delta x^2/(4D)$ is satisfied), and the overall algorithm (fast diffusion updates, slow daily cell events) is summarised in the flowchart of Figure 1. All parameters are declared as constants in the Fortran 90 source code (provided as supplementary material), and the random seed is fixed to 12345 to ensure full reproducibility. Thus, the on-lattice / off-lattice problem is resolved in a mathematically consistent and numerically stable manner.

A mathematical examination for stability of explicit finite difference method has been carried for $D = 2.5 \times 10^{-5}\text{cm}^2/\text{s}$, $N = 101$, $L = 0.5$ cm, $\Delta x = 0.005$ and $\Delta t \leq (\Delta x)^2/(4D) = 0.25$. The results show the stability of finite difference method. This model also uses some estimated values

for parameters which each one has a specific range. To show that this model is universal for these parameters, we have provided four other cases in different conditions presented in Table 2 and their obtained results for diameter, the contribution of proliferating and necrotic cells and the number of total cells in tumor has been summarized in Table 3. The prepared data in Table 3 illustrates that if σ_θ is limited and came down, the tumor size will increase since this restriction leads the newborn cells to the edge of tumor and these cells have lesser probability to move to tumor inside. Decreasing in $\boldsymbol{\delta_{th}^{Q\to N}}$, owing to the higher probability for proliferation and lower chance for necrosing, shows an increase in the number of cells in tumor. These results are comparable and the variation in parameters do not make a strong change in the results. Thus, it sounds that these variations maintain the universal tumor features such as structure, tumor size and the total number of tumor cells.

In order to validate our model and obtained results, the comparison with experimental data prepared in [52], which investigates the progression of avascular tumors, was carried out. In this manner, we plot Figure 8b, whose trend is consistent with the reported results in this work. As a detailed comparison, the tumor volume is around ~0.5–1 mm³ after 25 days, which is in agreement with the results presented in Figure 8b. In addition, the diameter of the necrotic core in our model is about ~600–700 μm, in agreement with the experimental reported in [52]. Based on a microfluidic study for examination of tumor evaluation in initial days [48], the tumor volume is ~0.01–0.04 mm³ for days 3–8. The presented model, under different conditions, gives ~0.01–0.05 mm³, which lies within the acceptable range relative to the experimental data.

Conclusion

In this study, a probabilistic mathematical model of avascular tumor growth was formulated. The model is based on solving a nonlinear coupled system of diffusion equations for O_2 and CO_2, incorporating cellular metabolic criteria to guide stochastic parameter choices. Stochastic methods were employed for phenotype transitions and for determining the placement of daughter cells. Simulations were performed over 40 days with a doubling time of 24 hours. The results show that the model spontaneously forms a necrotic core surrounded by quiescent and proliferative shells. Hypoxia-driven quiescent and necrotic cells emerge around days 9 and 10, respectively, coinciding with abrupt changes in the average O_2 and CO_2 concentrations in the microenvironment. Asymmetric diffusion of the two gases is evident due to random tumor expansion in different directions. Over the simulation period, the total cell count increases to approximately 4×10^4. Phenotypic diversity, measured via Shannon entropy, peaks around day 12 (consistent with the PCI result) and then declines as the necrotic fraction grows. The time derivative dH_{Ph}/dt captures phenotype transition rates and reflects the dynamics of the microenvironment.

We emphasize that these findings are qualitative and should not be overinterpreted as precise clinical predictions; the model is intended as a proof-of-concept and a hypothesis-generating tool. Several extensions are necessary to move toward more realistic and predictive applications. First, the framework should be extended to three spatial dimensions to better capture tumor geometries

and anisotropic growth patterns. Second, the inclusion of angiogenesis is critical to model the transition from avascular to vascularized tumors and the resulting changes in nutrient supply. Third, immune cell interactions (both innate and adaptive) should be incorporated to study how the immune system modulates tumor progression and treatment response. Additional future directions include coupling the model with drug delivery kinetics and calibrating parameters using patient-specific imaging data. With these enhancements, the present modular framework can serve as a quantitative tool for hypothesis testing and experimental design, while always acknowledging its inherent limitations.

Declaration of Competing Interest

The authors declare that they have no known competing financial interests or personal relationships that could have appeared to influence the work reported in this paper.

Compliance with ethical standards

Conflict of interest: The authors declare no conflict of interest.

Data Availability:

All the data produced or examined in this study are incorporated into this article.

Authors' Contribution: H.R.M. Zarandi & F. Sadeghi conceptualized the study and developed the mathematical model. H.R.M. Zarandi wrote the simulation code and performed the numerical experiments. All authors analyzed the results and drafted the manuscript, reviewed and approved the final version.

Ethical Approval: This study did not involve human participants, animal experiments, or clinical samples.

Funding: This research received no specific grant from any funding agency in the public, commercial, or not-for-profit sectors.

Informed Consent: No human subjects were involved in this study.

References

1. Ma'ayan, A., *Complex systems biology.* Journal of The Royal Society Interface, 2017. **14**(134): p. 20170391.
2. Mesquita, M.V., A.R. Vasconcellos, and R. Luzzi, *Complexity in biological systems.* Contemporary Physics, 1999. **40**(4): p. 247-256.
3. M, M., et al., *Cytotoxicity and targeted drug delivery of green synthesized metallic nanoparticles against oral Cancer: A review.* Inorganic Chemistry Communications, 2025. **173**: p. 113806.
4. Dykman, L., B. Khlebtsov, and N. Khlebtsov, *Drug delivery using gold nanoparticles.* Advanced Drug Delivery Reviews, 2025. **216**: p. 115481.
5. Yang, P., et al., *Numerical modeling and simulation for microneedles drug delivery: A novel comprehensive swelling-obstruction-mechanics model.* European Journal of Pharmaceutics and Biopharmaceutics, 2025. **206**: p. 114583.
6. Gas, P., M. Suleman, and F. Khaliq, *3D Computational Modeling of Fe3O4@Au Nanoparticles in Hyperthermia Treatment of Skin Cancer.* Nanotechnology, Science and Applications, 2025. **18**(null): p. 173-196.
7. Sharma, N., et al., *Experimental analysis of metamaterial integrated applicator for hyperthermia cancer treatment.* Scientific Reports, 2025. **15**(1): p. 18771.
8. Duswald, T., et al., *Bridging scales: A hybrid model to simulate vascular tumor growth and treatment response.* Computer Methods in Applied Mechanics and Engineering, 2024. **418**: p. 116566.
9. Sadhukhan, S. and S.K. Basu, *Avascular tumour growth models based on anomalous diffusion.* Journal of Biological Physics, 2020. **46**(1): p. 67-94.
10. Sadhukhan, S. and P.K. Mishra, *A multi-layered hybrid model for cancer cell invasion.* Medical & Biological Engineering & Computing, 2022. **60**(4): p. 1075-1098.
11. Sadhukhan, S., et al., *A multi-scale agent-based model for avascular tumour growth.* Biosystems, 2021. **206**: p. 104450.
12. Chaplain, M.A.J., *Avascular growth, angiogenesis and vascular growth in solid tumours: The mathematical modelling of the stages of tumour development.* Mathematical and Computer Modelling, 1996. **23**(6): p. 47-87.
13. Pourhasanzade, F., et al., *An agent-based model of avascular tumor growth: Immune response tendency to prevent cancer development.* SIMULATION, 2017. **93**(8): p. 641-657.
14. Tang, L., et al., *Computational Modeling of 3D Tumor Growth and Angiogenesis for Chemotherapy Evaluation.* PLOS ONE, 2014. **9**(1): p. e83962.
15. Abajian, A.C. and J. Lowengrub, *An agent-based hybrid model for avascular tumor growth.* The UC Irvine Undergraduate Research Journal, 2008. **11**: p. 1-12.
16. Ferreira, S.C., M.L. Martins, and M.J. Vilela, *Reaction-diffusion model for the growth of avascular tumor.* Physical Review E, 2002. **65**(2): p. 021907.
17. Betancourt-Padron, P., et al., *Phase transition in tumor growth VIII: The spatiotemporal avascular evolution.* Revista mexicana de física, 2020. **66**(6): p. 856-862.
18. Anderson, A.R.A., et al., *Mathematical Modelling of Tumour Invasion and Metastasis.* Computational and Mathematical Methods in Medicine, 2000. **2**(2): p. 490902.
19. Walenta, S., et al., *High Lactate Levels Predict Likelihood of Metastases, Tumor Recurrence, and Restricted Patient Survival in Human Cervical Cancers1.* Cancer Research, 2000. **60**(4): p. 916-921.

20. Pompa, M., et al. *An Agent-Based Model of Avascular Tumor Growth*. in *2024 IEEE 24th International Symposium on Computational Intelligence and Informatics (CINTI)*. 2024.
21. Mahmood, M.S., S. Mahmood, and D. Dobrota, *Formulation and numerical simulations of a continuum model of avascular tumor growth.* Mathematical Biosciences, 2011. **231**(2): p. 159-171.
22. Al-Mekhlafi, S.M., *Numerical simulation of hybrid deterministic-stochastic PDE models for cancer tumor growth.* Research in Mathematics, 2025. **12**(1): p. 2567717.
23. Debbouche, N., et al., *Chaos in Cancer Tumor Growth Model with Commensurate and Incommensurate Fractional-Order Derivatives.* Computational and Mathematical Methods in Medicine, 2022. **2022**(1): p. 5227503.
24. Jiang, N., L. Liu, and H. Yu, *Efficient stochastic asymptotic-preserving scheme for tumor growth models with uncertain parameters.* Journal of Computational and Applied Mathematics, 2026. **473**: p. 116881.
25. Jacobs, M., I. Kim, and J. Tong, *Tumor growth with nutrients: regularity and stability.* Communications of the American Mathematical Society, 2023. **3**(04): p. 166-208.
26. Strong, S.P., et al., *Entropy and Information in Neural Spike Trains.* Physical Review Letters, 1998. **80**(1): p. 197-200.
27. Izquierdo-Kulich, E., E. Alonso-Becerra, and J.M. Nieto-Villar, *Entropy production rate for avascular tumor growth.* Journal of Modern Physics, 2011. **2**(6): p. 615-620.
28. Legaria-Peña, J.U., F. Sánchez-Morales, and Y. Cortés-Poza, *Evaluation of entropy and fractal dimension as biomarkers for tumor growth and treatment response using cellular automata.* Journal of Theoretical Biology, 2023. **564**: p. 111462.
29. Shannon, C.E., *A mathematical theory of communication.* The Bell System Technical Journal, 1948. **27**(3): p. 379-423.
30. Cover, T.M., *Elements of information theory*. 1999: John Wiley & Sons.
31. Eskov, V.M., et al., *Shannon entropy in the research on stationary regimes and the evolution of complexity.* Moscow University Physics Bulletin, 2017. **72**(3): p. 309-317.
32. Batty, M., et al., *Entropy, complexity, and spatial information.* Journal of Geographical Systems, 2014. **16**(4): p. 363-385.
33. Bergstrom, C.T. and M. Lachmann. *Shannon information and biological fitness*. in *Information Theory Workshop*. 2004.
34. Adami, C., *Information theory in molecular biology.* Physics of Life Reviews, 2004. **1**(1): p. 3-22.
35. Conforte, A.J., et al., *Signaling Complexity Measured by Shannon Entropy and Its Application in Personalized Medicine.* Frontiers in Genetics, 2019. **Volume 10 - 2019**.
36. West, J., et al., *On dynamic network entropy in cancer.* arXiv preprint arXiv:1202.3015, 2012.
37. Jaynes, E.T., *Information Theory and Statistical Mechanics. II.* Physical Review, 1957. **108**(2): p. 171-190.
38. Hanahan, D. and Robert A. Weinberg, *Hallmarks of Cancer: The Next Generation.* Cell, 2011. **144**(5): p. 646-674.
39. Sood, A.K., et al., *The clinical significance of tumor cell-lined vasculature in ovarian carcinoma: implications for anti-vasculogenic therapy.* Cancer biology & therapy, 2002. **1**(6): p. 661-664.

40. Gilkes, D.M., G.L. Semenza, and D. Wirtz, *Hypoxia and the extracellular matrix: drivers of tumour metastasis.* Nature Reviews Cancer, 2014. **14**(6): p. 430-439.
41. Semenza, Gregg L., *Hypoxia-Inducible Factors in Physiology and Medicine.* Cell, 2012. **148**(3): p. 399-408.
42. Swietach, P., et al., *The chemistry, physiology and pathology of pH in cancer.* Philosophical Transactions of the Royal Society B: Biological Sciences, 2014. **369**(1638): p. 20130099.
43. Garg, A.D., et al., *DAMPs and PDT-mediated photo-oxidative stress: exploring the unknown.* Photochemical & Photobiological Sciences, 2011. **10**(5): p. 670-680.
44. Thomlinson, R.H. and L.H. Gray, *The histological structure of some human lung cancers and the possible implications for radiotherapy.* Br J Cancer, 1955. **9**(4): p. 539-49.
45. Rofstad, E.K., et al., *Hypoxia Promotes Lymph Node Metastasis in Human Melanoma Xenografts by Up-Regulating the Urokinase-Type Plasminogen Activator Receptor1.* Cancer Research, 2002. **62**(6): p. 1847-1853.
46. Ilina, O., et al., *Cell–cell adhesion and 3D matrix confinement determine jamming transitions in breast cancer invasion.* Nature Cell Biology, 2020. **22**(9): p. 1103-1115.
47. Taghibakhshi, A., et al., *Three-dimensional modeling of avascular tumor growth in both static and dynamic culture platforms.* Micromachines, 2019. **10**(9): p. 580.
48. Ziółkowska, K., et al. *Long-term Multicellular Spheroids culture and anticancer drug activity evaluation in a microfluidic system*. in *Proc. MicroTAS*. 2011.
49. Patra, B., et al., *Drug testing and flow cytometry analysis on a large number of uniform sized tumor spheroids using a microfluidic device.* Scientific reports, 2016. **6**(1): p. 21061.
50. Kwapiszewska, K., et al., *A microfluidic-based platform for tumour spheroid culture, monitoring and drug screening.* Lab on a Chip, 2014. **14**(12): p. 2096-2104.
51. Moshksayan, K., et al., *Spheroids-on-a-chip: Recent advances and design considerations in microfluidic platforms for spheroid formation and culture.* Sensors and Actuators B: Chemical, 2018. **263**: p. 151-176.
52. Freyer, J.P. and R.M. Sutherland, *Regulation of growth saturation and development of necrosis in EMT6/Ro multicellular spheroids by the glucose and oxygen supply.* Cancer research, 1986. **46**(7): p. 3504-3512.
53. Jiang, Y., et al., *A Multiscale Model for Avascular Tumor Growth.* Biophysical Journal, 2005. **89**(6): p. 3884-3894.
54. Anderson, A.R. and M.A. Chaplain, *Continuous and discrete mathematical models of tumor-induced angiogenesis.* Bulletin of mathematical biology, 1998. **60**(5): p. 857-899.
55. Hassan, S.S. and H.M. Al-Saedi, *Tumour Chemotherapy by Continuous Infusion Drug Using Exponential Growth.* Journal of Engineering, 2025. **31**(6): p. 149-172.
56. Anderson, A.R., et al., *Tumor morphology and phenotypic evolution driven by selective pressure from the microenvironment.* Cell, 2006. **127**(5): p. 905-915.
57. Gatenby, R.A. and R.J. Gillies, *Why do cancers have high aerobic glycolysis?* Nature reviews cancer, 2004. **4**(11): p. 891-899.
58. Balázsi, G., A. Van Oudenaarden, and J.J. Collins, *Cellular decision making and biological noise: from microbes to mammals.* Cell, 2011. **144**(6): p. 910-925.
59. Roussos, E.T., J.S. Condeelis, and A. Patsialou, *Chemotaxis in cancer.* Nature Reviews Cancer, 2011. **11**(8): p. 573-587.

60. Vital-Lopez, F.G., et al., *Modeling the effect of chemotaxis on glioblastoma tumor progression.* AIChE journal, 2011. **57**(3): p. 778-792.
61. Sanoria, M., et al., *Chemotaxis-driven instabilities govern size, shape and migration efficiency of multicellular clusters.* PRX Life, 2026. **4**(1): p. 013004.
62. Codling, E.A., M.J. Plank, and S. Benhamou, *Random walk models in biology.* Journal of the Royal society interface, 2008. **5**(25): p. 813-834.
63. Noble, P., *Extracellular matrix and cell migration: locomotory characteristics of MOS-11 cells within a three-dimensional hydrated collagen lattice.* Journal of Cell Science, 1987. **87**(2): p. 241-248.
64. Grote, J., R. Süsskind, and P. Vaupel, *Oxygen diffusivity in tumor tissue (DS-Carcinosarcoma) under temperature conditions within the range of 20–40°C.* Pflügers Archiv, 1977. **372**(1): p. 37-42.
65. Vaupel, P. and H. Piazena. *Hyperhydration of Cancers: A Characteristic Biophysical Trait Strongly Increasing O2, CO2, Glucose and Lactate Diffusivities, and Improving Thermophysical Properties of Solid Malignancies*. in *Oxygen Transport to Tissue XLIV*. 2023. Cham: Springer International Publishing.
66. Swietach, P., *What is pH regulation, and why do cancer cells need it?* Cancer and Metastasis Reviews, 2019. **38**(1): p. 5-15.
67. Grimes, D.R., et al., *A method for estimating the oxygen consumption rate in multicellular tumour spheroids.* Journal of The Royal Society Interface, 2014. **11**(92): p. 20131124.
68. Lin, F., et al., *Effects of a simulated CO2 pneumoperitoneum environment on the proliferation, apoptosis, and metastasis of cervical cancer cells in vitro.* Med Sci Monit, 2014. **20**: p. 2497-503.
69. MacKay, D.J., *Information theory, inference and learning algorithms*. 2003: Cambridge university press.
70. Shirinifard, A., et al., *3D Multi-Cell Simulation of Tumor Growth and Angiogenesis.* PLOS ONE, 2009. **4**(10): p. e7190.
71. Žnidar, V., *Modeling avascular tumour growth*. 2024, Sveučilište u Zagrebu, Sveučilište u Zagrebu Prirodoslovno-matematički ….
72. Blom, E. and S. Engblom, *Morphological stability for in silico models of avascular tumors.* Bulletin of Mathematical Biology, 2024. **86**(7): p. 75.
73. Liu, S., et al., *Simulation of avascular tumor growth and drug response in a microfluidic device with a cellular automaton model.* Microfluidics and Nanofluidics, 2024. **28**(4): p. 21.
74. Freyer, J.P. and R.M. Sutherland, *Regulation of Growth Saturation and Development of Necrosis in EMT6/Ro Multicellular Spheroids by the Glucose and Oxygen Supply1.* Cancer Research, 1986. **46**(7): p. 3504-3512.
75. Sutherland, R.M., *Cell and Environment Interactions in Tumor Microregions: The Multicell Spheroid Model.* Science, 1988. **240**(4849): p. 177-184.
76. Roose, T., S.J. Chapman, and P.K. Maini, *Mathematical Models of Avascular Tumor Growth.* SIAM Review, 2007. **49**(2): p. 179-208.
77. Gillies, R.J. and R.A. Gatenby, *Adaptive landscapes and emergent phenotypes: why do cancers have high glycolysis?* Journal of Bioenergetics and Biomembranes, 2007. **39**(3): p. 251-257.

78. Smallbone, K., et al., *Metabolic changes during carcinogenesis: Potential impact on invasiveness.* Journal of Theoretical Biology, 2007. **244**(4): p. 703-713.